Optimization of three-dimensional electron diffuse scattering data acquisition

Romy Poppe[a] and Joke Hadermann[a]

[a]University of Antwerp, Department of Physics, Groenenborgerlaan 171, B-2020 Antwerp, Belgium

Correspondence email: romy.poppe@uantwerpen.be

Funding information: Financial support is acknowledged from the University of Antwerp through BOF TOP 38689 and FWO G035619N.

Abstract: The diffraction patterns of crystalline materials with local order contain sharp Bragg reflections as well as highly structured diffuse scattering. In this study, we quantitatively show how the diffuse scattering in three-dimensional electron diffraction (3D ED) data is influenced by various parameters, including the data acquisition mode, the detector type and the use of an energy filter. We found that diffuse scattering data used for quantitative analysis are preferably acquired in selected area electron diffraction (SAED) mode using a CCD and an energy filter. In this study, we also show that the diffuse scattering in 3D ED data can be obtained with a quality comparable to that from single-crystal X-ray diffraction. As electron diffraction requires much smaller crystal sizes than X-ray diffraction, this opens up the possibility to investigate the local structure of many technologically relevant materials for which no crystals large enough for single-crystal X-ray diffraction are available.

Keywords: 3D electron diffraction; single-crystal diffuse scattering

1. Introduction

Diffraction patterns of crystalline materials contain sharp Bragg reflections, arising from the periodicity of the crystalline lattice, and weak diffuse scattering, arising from the disorder. Diffuse scattering occurs whenever there are deviations from the average structure – that is, when the crystal is disordered. When the deviations from the average structure are ordered on a local scale, they give rise to highly structured diffuse scattering. Examples of parameters that can be refined from the intensity distribution of the diffuse scattering are the number of stacking faults, correlations between neighbouring atoms and local atomic displacements. Because the properties of many materials do not only depend on the average structure, but also on the disorder, quantitative analysis of diffuse scattering is essential for understanding and optimizing material properties.

In this article, we discuss the acquisition procedure of three-dimensional electron diffraction (3D ED) data containing diffuse scattering. The development of 3D ED in 2007 (Kolb *et al.*, 2007, 2008) allowed to determine the crystal structure of materials for which no crystals large enough for single-crystal X-ray diffraction are available (Gemmi *et al.*, 2019). The diffuse scattering in single-crystal

electron diffraction data has been analysed both qualitatively (for example, Withers et al., 2003, 2004; Fujii et al., 2007; Goodwin et al., 2007; Brázda et al., 2016; Zhao et al., 2017; Neagu & Tai, 2017; Gorelik et al., 2023) and quantitatively (Krysiak et al., 2018, 2020; Poppe et al., 2022, 2024; Schmidt et al., 2023). For the quantitative analysis of diffuse scattering, high-quality diffuse scattering data are needed. The instrumental requirements and data processing techniques for obtaining high-quality diffuse scattering data have previously been determined for X-ray and neutron diffraction (Welberry & Weber, 2016), but not yet for electron diffraction, which is the scope of this study.

2. Experimental section

The samples that were used in this study were previously studied in (Roth *et al.*, 2021; Poppe *et al.*, 2024) and will be referred to as the 'SC-0.81' and 'Q-0.84 #2' samples. The 'Q-0.84 #2' sample (nominal stoichiometry $Nb_{0.84}CoSb$) was thermally quenched (Q) from the melt and only has short-range Nb-vacancy order. The 'SC-0.81' sample (nominal stoichiometry $Nb_{0.81}CoSb$) was slowly cooled (SC) using an induction furnace and has long-range Nb-vacancy order.

Samples for electron diffraction data collection were prepared by dispersing the powder in ethanol. A few droplets of the suspension were deposited on a copper grid covered with an amorphous carbon film. Ultra-thin amorphous carbon grids with a thickness of 3-4 nm from Electron Microscopy Sciences were used to reduce the background originating from the carbon film.

In-zone selected area electron diffraction (SAED) and in-zone precession electron diffraction (PED) patterns were acquired with an FEI Tecnai G2 electron microscope operated at 200 kV using an FEI Eagle 2k CCD camera (2048 x 2048 pixels with 16-bit dynamic range). In-zone PED patterns were acquired with a DigiSTAR precession device from NanoMEGAS and using a precession angle of 1°.

Three-dimensional electron diffraction (3D ED) data were acquired with an aberration-corrected cubed FEI Titan 80-300 electron microscope operated at 300 kV using a GATAN US1000XP CCD camera (4096 x 4096 pixels with 16-bit dynamic range). One 3D ED data set was acquired using a Quantum Detectors MerlinEM hybrid pixel detector (512 x 512 pixels with 24-bit dynamic range). The crystals were illuminated in SAED mode with an exposure time of 1 s per frame. Electron diffraction patterns were acquired with a Fischione tomography holder (tilt range of ±80°), in a stepwise manner, using an in-house developed script. The 3D ED data were collected with a step size of 0.1° on crystals with a size of 200-3000 nm. For the larger crystals, only a thin part of the crystal was illuminated, which was recentred inside the aperture every few degrees. Energy filtered 3D ED data were acquired with a Quantum 966 Gatan Image Filter, with a slit width of 10 eV.

PETS2 (Palatinus *et al.*, 2019) was used to process the 3D ED data including background subtraction of the individual frames and applying symmetry with Laue class $m\bar{3}m$ in the reconstruction of the three-dimensional reciprocal lattice. The three-dimensional reciprocal lattice of all 3D ED data was

indexed with a cubic unit cell with space group $F\bar{4}3m$ and cell parameter a = 5.89864(3) Å, which was previously determined by Zeier et al. using synchrotron powder X-ray diffraction (Zeier *et al.*, 2017).

To quantitatively determine the effect of various experimental parameters on the diffuse scattering, the observed diffuse scattering was compared with the diffuse scattering calculated for the short-range order parameters refined using a Monte Carlo refinement in *DISCUS* (Proffen & Neder, 1997) and previously published in (Poppe *et al.*, 2024). The R value

$$R_w = \sqrt{\frac{\sum_i w_i [I_{\mathrm{obs}}(\mathbf{Q}_i) - I_{\mathrm{calc}}(\mathbf{Q}_i)]^2}{\sum_i w_i [I_{\mathrm{obs}}(\mathbf{Q}_i)]^2}} \quad (1)$$

was calculated using an in-house developed script. The summation is over all measured reciprocal lattice points $\mathbf{Q}_i$, I_{obs} and I_{calc} are the observed and calculated diffuse scattering intensities. The weights w_i were set to unity so that all data points *i* contribute equally to the summation. The experimental and calculated electron diffraction patterns were scaled and a constant background was subtracted. The Bragg reflections were subtracted and the size of the circular mask covering the central beam was systematically adjusted until the R value reached its minimum.

Details on the acquisition of the single-crystal X-ray diffraction data can be found in (Roth *et al.*, 2021).

3. Results and discussion

3.1. Symmetry averaging

Fig. 1 shows the *h0l* and *hhl* planes reconstructed from 3D ED data before and after applying symmetry averaging with Laue class $m\bar{3}m$. The *h0l* and *hhl* planes before applying symmetry averaging have a missing wedge due to the limited tilt range (90° for the thermally quenched sample (Q-0.84 #2) and 100° for the slowly cooled sample (SC-0.81)). Applying symmetry averaging with Laue class $m\bar{3}m$ allows to fill the missing wedge in the three-dimensional reciprocal lattice, which is required for the calculation of the three-dimensional difference pair distribution function (3D-ΔPDF) (Schmidt et al., 2023). The 3D-ΔPDF is a method that is often used to determine the origin of the diffuse scattering (Schaub *et al.*, 2007). For samples where symmetry averaging does not allow to fill the missing wedge completely, full reciprocal space coverage could be achieved by combining several data sets from the same crystal acquired with a different orientation of the grid in the sample holder. Combining data sets from several crystals is not recommended since not all crystals have identical diffuse scattering (Fig. S1). All crystals have satellite reflections on top of the diffuse scattering, but their sharpness is different. The sharpness of the satellite reflections is related to the correlation length of the local Nb-vacancy order. Crystals with long-range Nb-vacancy order consist of twins with different orientations (Xia *et al.*, 2019). Each twin orientation gives rise to one pair of satellite reflections. The 3D ED data for the slowly cooled sample (SC-0.81) in Fig. 1 were acquired on a 150

nm sized crystal. Not all satellite reflections are visible in the *h0l* and *hhl* planes before symmetry averaging, which indicates that some twin orientations are missing. Fig. 1 shows that symmetry averaging with Laue class $m\bar{3}m$ introduces additional satellite reflections corresponding to the other twin orientations. For crystals with long-range Nb-vacancy order, symmetry averaging is thus only valid when the volume percentages of the different twin orientations in the crystal are quasi identical. For the quenched sample, the satellite reflections are less sharp, which indicates that the correlation length of the Nb-vacancy order is smaller than for the slowly cooled sample.

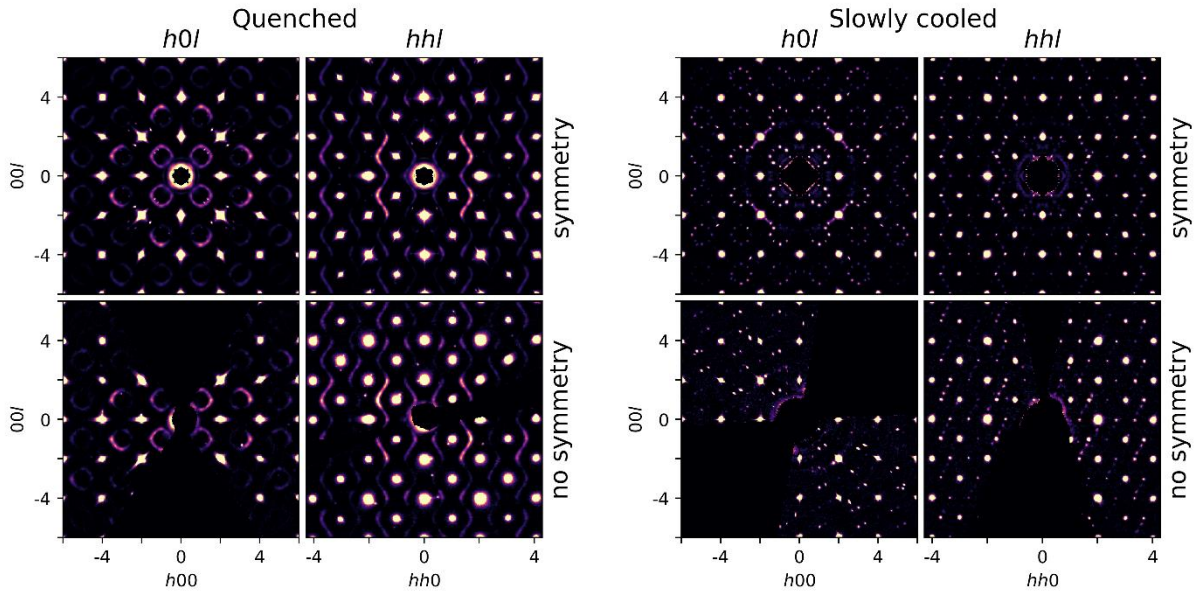

Figure 1 Comparison of the *h0l* and *hhl* planes reconstructed from three-dimensional electron diffraction (3D ED) data before and after applying symmetry averaging with Laue class $m\bar{3}m$, both for the thermally quenched sample (Q-0.84 #2) and the slowly cooled sample (SC-0.81). The additional reflections between the Bragg reflections are due to neighbouring crystals. Due to symmetry averaging with Laue class $m\bar{3}m$, each additional reflection in the *h0l* plane will appear eight times, while each additional reflection in the *hhl* plane will appear four times.

3.2. Three-dimensional electron diffraction vs. in-zone selected area electron diffraction

Three-dimensional electron diffraction (3D ED) allows to acquire three-dimensional electron diffuse scattering data with less multiple scattering compared to in-zone selected area electron diffraction (SAED) patterns. Another method that is often used to record the intensities of the Bragg reflections with reduced multiple scattering is precession electron diffraction (PED) (Vincent & Midgley, 1994). In PED, the electron beam is tilted away from the optical axis of the electron microscope by a certain angle (the precession angle, typically 1-3°) and rotated on the surface of a cone with the vertex fixed on the sample plane. The resulting PED pattern is obtained by integrating the intensities in the acquired off-axis electron diffraction patterns. When the crystal is oriented along a zone-axis, and the

electron beam is tilted away from this zone-axis, the total number of possible multiple diffraction paths is reduced, and consequently also the amount of multiple scattering.

Fig. 2 shows the *h0l* plane reconstructed from 3D ED data, the [010] in-zone SAED pattern, and the [010] in-zone PED pattern acquired on the same crystal of the thermally quenched sample (Q-0.84 #2), before and after applying symmetry averaging with Laue class $m\bar{3}m$. The diffuse circles in the *h0l* plane reconstructed from 3D ED show clear intensity modulations. In contrast, the diffuse circles in the in-zone SAED pattern have almost the same intensity everywhere due to multiple scattering. The intensity distribution of the diffuse scattering in the in-zone PED pattern is very similar to the one in the in-zone SAED pattern. The main difference is that the higher-order Bragg reflections have higher intensities in the in-zone PED pattern than in the in-zone SAED pattern. Bragg reflections are distinct points, whereas diffuse scattering is continuously distributed in reciprocal space. In-zone PED patterns are obtained by integrating the intensities within a volume in reciprocal space (determined by the precession angle). Consequently, higher precession angles will decrease the resolution of the observed diffuse scattering.

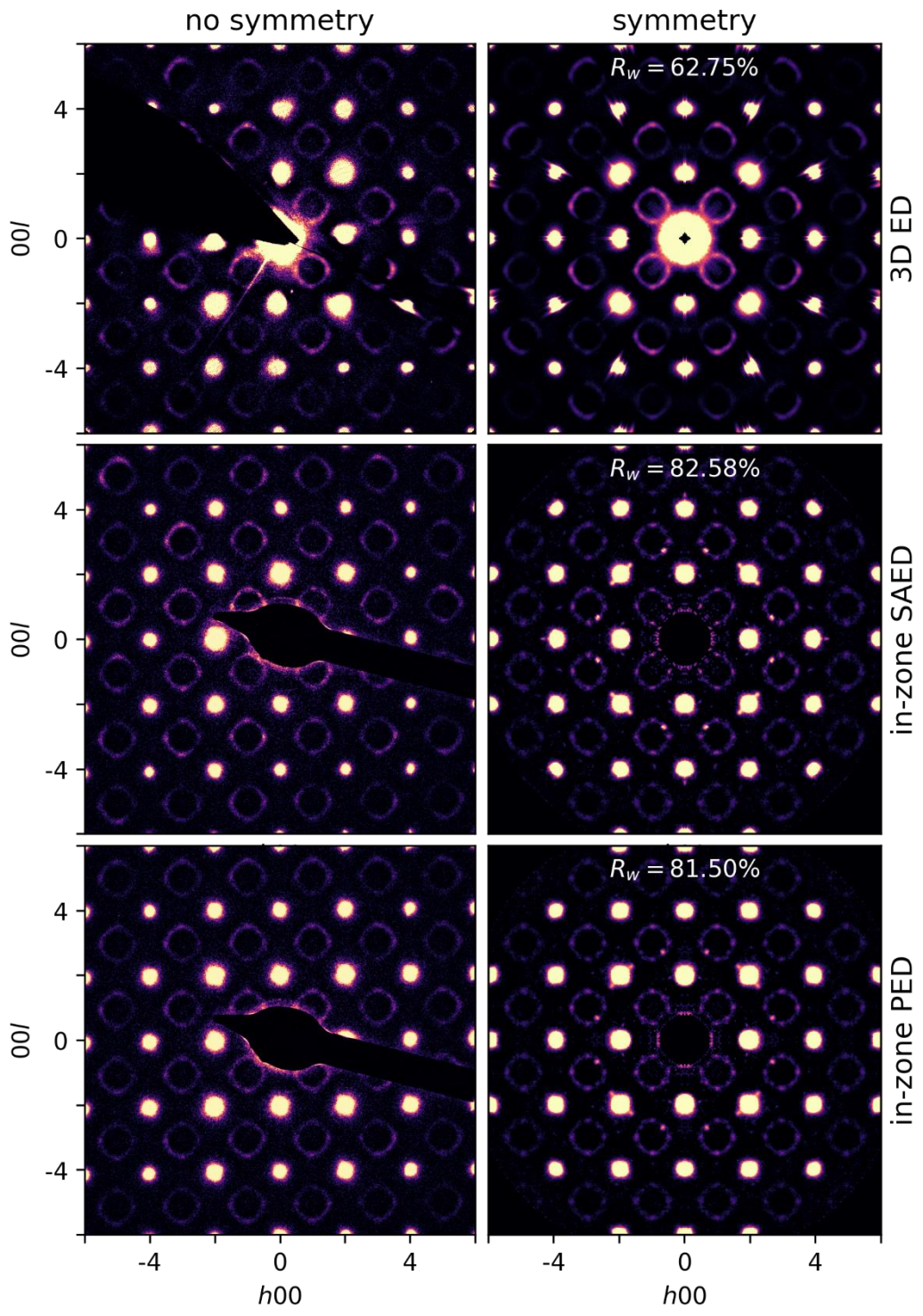

Figure 2 Comparison of the *h0l* plane reconstructed from three-dimensional electron diffraction (3D ED) data, the [010] in-zone selected area electron diffraction (SAED) pattern, and the [010] in-zone precession electron diffraction (PED) pattern acquired on the same crystal, before and after applying symmetry averaging with Laue class $m\bar{3}m$. Data acquired on the thermally quenched sample (Q-0.84 #2).

The diffuse scattering in the *h0l* plane reconstructed from 3D ED data, the [010] in-zone SAED pattern, and the [010] in-zone PED patterns in Fig. 2 was compared with the diffuse scattering calculated for the short-range order parameters previously refined using a Monte Carlo refinement in *DISCUS* (Poppe *et al.*, 2024) and shown in Fig. S2. The R value in Equation 1 was calculated for the electron diffraction patterns in Fig. 2 after applying symmetry averaging with Laue class $m\bar{3}m$. For the *h0l* plane reconstructed from 3D ED data, the R value ($R_w = 62.75\%$) is systematically lower compared to the R value for the in-zone SAED pattern ($R_w = 82.58\%$) and the in-zone PED pattern ($R_w = 81.50\%$). As the diffuse scattering in Fig. S2 is calculated in the kinematical approximation, this shows that the diffuse scattering in 3D ED data is less influenced by multiple scattering compared to the diffuse scattering in in-zone SAED and in-zone PED patterns. It should be noted that R values higher than 60% are normal for the diffuse scattering in 3D ED data (Poppe et al., 2022, 2024).

The 3D ED data in Fig. 2 were acquired using a tilt step of 0.1°, which is close to the accuracy of the TEM goniometer. Fig. 3 shows the effect of the tilt step on the diffuse scattering in the *h0l* and *hhl* planes reconstructed from the 3D ED data in Fig. 2. The larger the tilt step, the larger the missing wedge between two subsequent frames. Acquiring 3D ED data in continuous mode does not fill the missing wedge between two subsequent frames since the three-dimensional reciprocal lattice is reconstructed from the individual frames. The synchrotron single-crystal X-ray diffraction data in Fig. 7 were also acquired in step size mode with a tilt step of 0.1°.

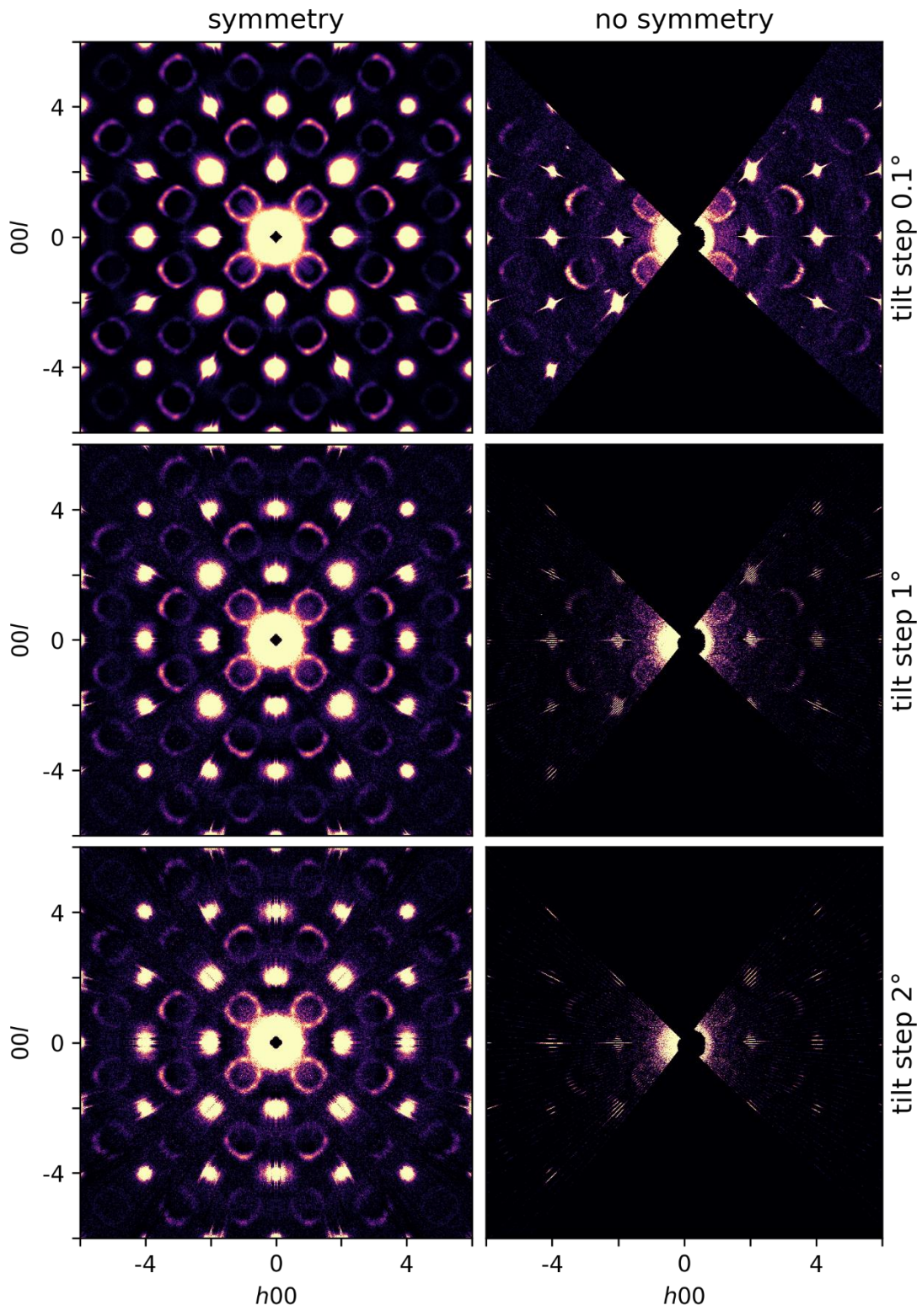

Figure 3 Comparison of the *h0l* and *hhl* planes reconstructed from three-dimensional electron diffraction (3D ED) data acquired with a tilt step of respectively 0.1°, 1° and 2°. Data acquired on the thermally quenched sample (Q-0.84 #2).

3.3. Background subtraction and energy filtering

Bragg reflections are three orders of magnitude stronger than the diffuse scattering. Since the diffuse scattering is difficult to dissociate from the experimental background, the acquisition of high-quality diffuse scattering data requires careful background subtraction. Obtaining high-quality diffuse scattering data with negligible background contributions comprises three steps: (i) increasing intensities, (ii) reducing the experimental background and (iii) post-experimental elimination of the background (Welberry & Weber, 2016). For the 3D ED data in Fig. 2, the background of the individual frames has been subtracted in *PETS2* before the reconstruction of the three-dimensional reciprocal lattice. The background of the in-zone SAED patterns and in-zone PED patterns has also been subtracted using *PETS2*.

The background in electron diffraction data is due to inelastic scattering of the incoming electrons (thermal diffuse scattering), electrons scattered by the amorphous carbon film, and sensor intrinsic background noise of the CCD. Thermal diffuse scattering can be subtracted using an energy filter. Fig. 4 shows the *h0l* plane reconstructed from 3D ED data acquired with and without energy filter on the same crystal. The energy filter blocks inelastically scattered electrons with an energy loss of more than 10 eV. Except for using an energy filter, the experimental settings were identical for both 3D ED data sets. The *h0l* plane reconstructed from 3D ED data acquired without energy filter shows strong diffuse intensity bands. The diffuse intensity bands are weaker in the *h0l* plane reconstructed from 3D ED data acquired with energy filter but can still be observed. An energy filter with a slit width of 10 eV reduces the thermal diffuse scattering but does not entirely remove it. The *h0l* planes after background subtraction in *PETS2* are also shown in Fig. 4. After background subtraction in *PETS2*, the *hhl* plane looks similar for the energy-filtered and non-energy filtered data. The experimental background and the thermal diffuse scattering are subtracted, while the elastic diffuse scattering remains. For the diffuse scattering in each of the electron diffraction patterns in Fig. 4 the R value in Equation 1 was calculated. The lowest R value was obtained for the *h0l* plane reconstructed from 3D ED data acquired with energy filter and without background subtraction in *PETS2* ($R_w = 67.11\%$). A previous study on acquiring energy filtered 3D ED data showed that the R_1 value calculated from the Bragg reflections in 3D ED data acquired with energy filter was 10-30% lower (Yang *et al.*, 2022). Acquiring 3D ED data using an energy filter is thus the best method to obtain diffuse scattering data that can be used for quantitative analysis.

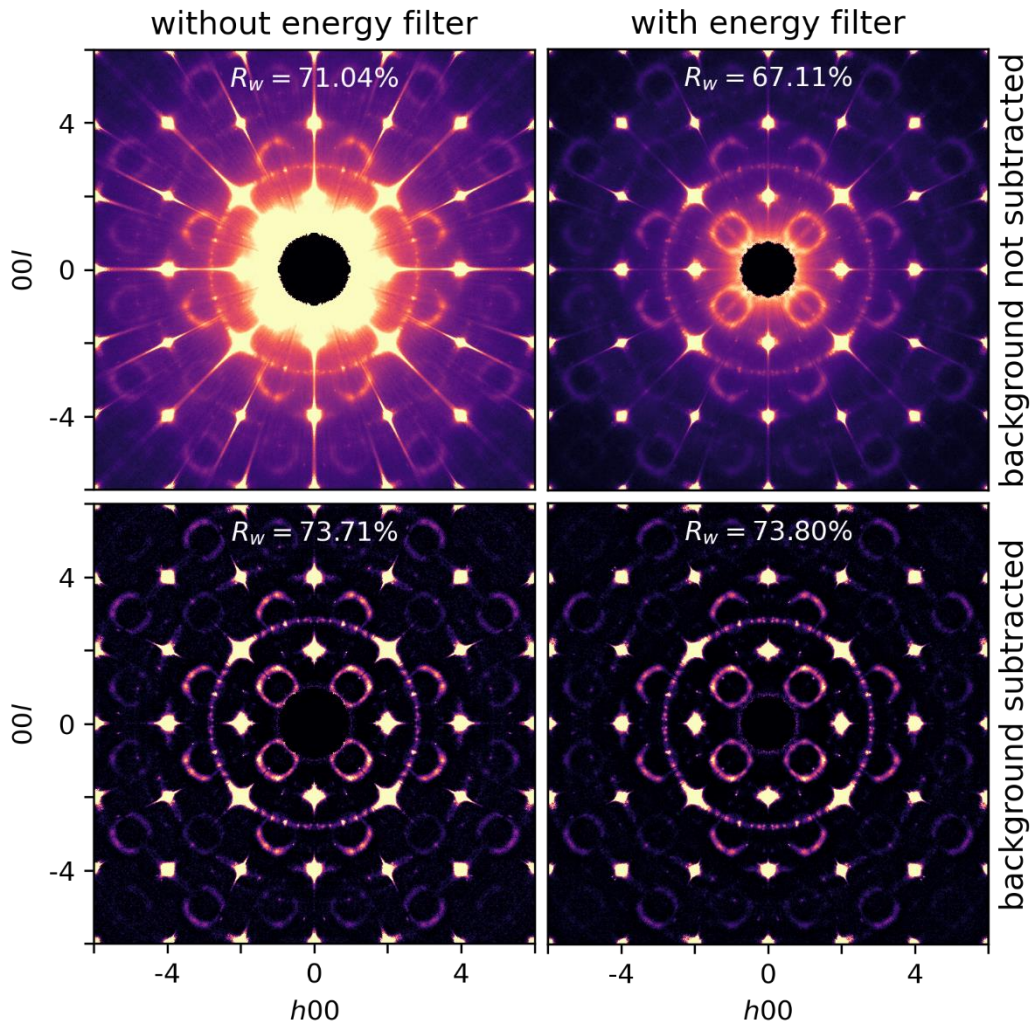

Figure 4 Comparison of the *h0l* plane reconstructed from three-dimensional electron diffraction (3D ED) data acquired with and without energy filter, before and after background subtraction in *PETS2*. The circle passing through the (202) Bragg reflection is due to neighbouring crystals. Due to symmetry averaging with Laue class $m\bar{3}m$, each additional reflection in the *h0l* plane will appear four times. Data acquired on the thermally quenched sample (Q-0.84 #2).

The background in *PETS2* was subtracted by using a median filter algorithm (Palatinus *et al.*, 2019). To ensure that the elastic diffuse scattering is not subtracted, the reflection size in *PETS2* should be chosen equal to or a bit larger than the width of the diffuse scattering contours (reflection size 20 in Fig. S3). When the reflection size is much lower than the width of the diffuse scattering contours, part of the elastic diffuse scattering will be subtracted.

Another method to estimate the background would be to repeat the 3D ED data acquisition under the same conditions but without the crystal illuminated by the electron beam. In the case of one-dimensional or two-dimensional diffuse scattering, the background intensity could also be estimated from the intensities of the surrounding voxels (Welberry & Weber, 2016). However, both methods do not subtract the thermal diffuse scattering, and would thus require energy-filtered 3D ED data.

3.4. Selected area electron diffraction vs. nano electron diffraction

In 3D ED, the crystal can be illuminated either in SAED mode or in nano electron diffraction (NED) mode (Zuo *et al.*, 2004). In SAED mode, the incident electron beam is parallel, and the sample area used for collecting diffraction data is determined by the selected area aperture. In NED mode, a small C2 condenser aperture is inserted, and the sample area used for collecting diffraction data is determined by the beam size. The incident electron beam in NED mode is usually slightly convergent. Fig. 5 shows the *h0l* and *hhl* planes reconstructed from 3D ED data acquired on the same crystal in SAED mode and in NED mode. The beam size in NED mode was chosen identical to the size of the selected area aperture in SAED mode (~ 700 nm). The electron beam in NED mode was quasi parallel (convergence angle of ~ 0.6°). The R value in Equation 1 was calculated for the diffuse scattering in each of the electron diffraction patterns in Fig. 5. The lowest R value was obtained for the 3D ED data acquired in SAED mode. However, since the intensity distribution of the diffuse scattering looks similar for the 3D ED data acquired in SAED and NED mode, the difference in R value is likely due to the different size of the central beam. To check if the different size of the central beam is indeed causing the difference in R value, the size of the circular mask covering the central beam was adjusted so that its size was identical for the 3D ED data acquired in SAED and in NED mode (Fig. S4). The R value is still lower for the *h0l* plane reconstructed from 3D ED data acquired in SAED mode but the difference in R value is smaller (79.19% vs 82.38%), indicating that the difference in R value is mainly due to the different size of the central beam. The 3D ED data in Fig. 5 were acquired on the quenched sample (Q-0.84 #2), while the 3D ED data in Fig. S4 were acquired on the slowly cooled sample (SC-0.81). The central beam is again larger for the 3D ED data acquired in NED mode. Besides, due to the slightly convergent electron beam in NED mode, the higher-order Bragg reflections in Fig. S5 have higher intensities for the 3D ED data acquired in NED mode than for the 3D ED data acquired in SAED mode. For the acquisition of diffuse scattering data, 3D ED data can thus best be acquired in SAED mode.

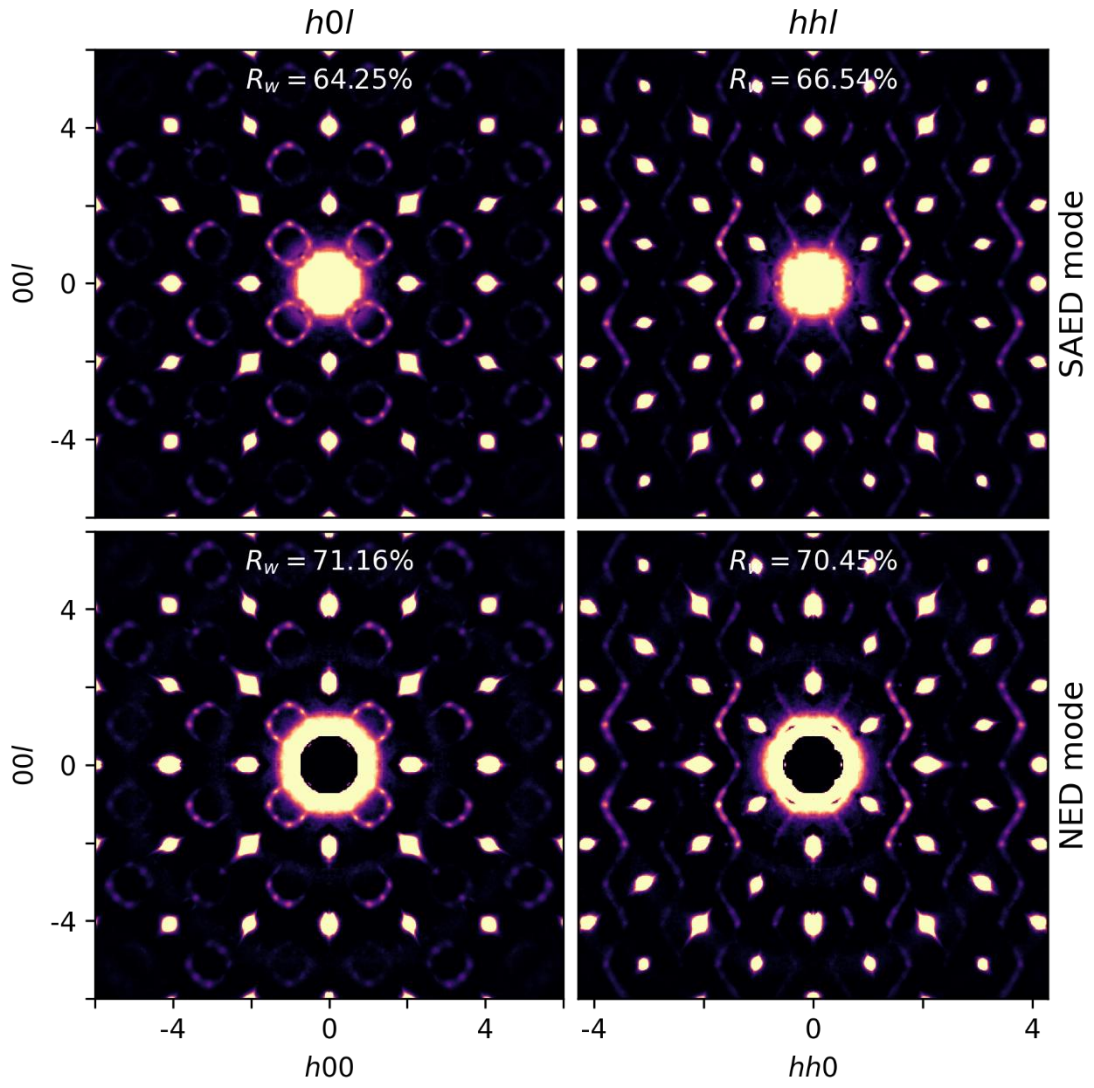

Figure 5 Comparison of the *h0l* and *hhl* planes reconstructed from three-dimensional electron diffraction (3D ED) data acquired in selected area electron diffraction (SAED) and nano electron diffraction (NED) mode. Data acquired on the thermally quenched sample (Q-0.84 #2).

3.5. Hybrid pixel detector vs. CCD

Important detector performance characteristics for diffuse scattering measurements include a narrow detector point spread function, low sensor intrinsic background noise, and a high dynamic range (Welberry & Weber, 2016). Hybrid pixel detectors such as Pilatus (Kraft *et al.*, 2009), XPAD (Pangaud *et al.*, 2008) or Medipix (Gimenez *et al.*, 2011) are used for the acquisition of high-quality single-crystal X-ray diffuse scattering data at synchrotron sources. The point spread function of hybrid pixel detectors at synchrotron sources is essentially one pixel broad, they can be operated under zero intrinsic noise conditions, and the dynamic range is higher than for CCDs (Welberry & Goossens, 2016).

Fig. 6 shows the *h0l* plane reconstructed from 3D ED data acquired with a GATAN US1000XP CCD camera and a Quantum Detectors MerlinEM hybrid pixel detector on the same crystal. The resolution of the observed diffuse scattering is worse for the 3D ED data acquired with the hybrid pixel detector than for the 3D ED data acquired with the CCD, which can be explained by a difference in the number of pixels between both detectors and a difference in the detector point spread function. The GATAN US1000XP CCD (4096 x 4096 pixels) has 64 times more pixels than the Quantum Detectors MerlinEM hybrid pixel detector (512 x 512 pixels). For electron diffraction, the detector point spread function is also larger for hybrid pixel detectors than for CCDs. Electrons are not directly detected by CCDs but are first converted to photons through a phosphor layer. The photons generate electron-hole pairs, and electrons are stored pixel-wise in potential wells of limited capacity. The point spread function of a CCD detector depends on the thickness of the phosphor layer (Welberry & Weber, 2016). Compared to CCDs, hybrid pixel detectors count electrons directly. Electrons that fall in on a hybrid pixel detector generate electron-hole pares in the silicon sensor. Incident electrons are detected by neighbouring pixels due to drift of incident electrons in the silicon sensor (Jakůbek, 2009). The point spread function of a hybrid pixel detector is larger for electrons with a higher energy. The X-rays used in a synchrotron source have a much lower energy compared to the electrons used in a TEM. The drift of X-rays in the silicon sensor of hybrid pixel detectors at synchrotron sources is negligible, and the point spread function is essentially one pixel broad.

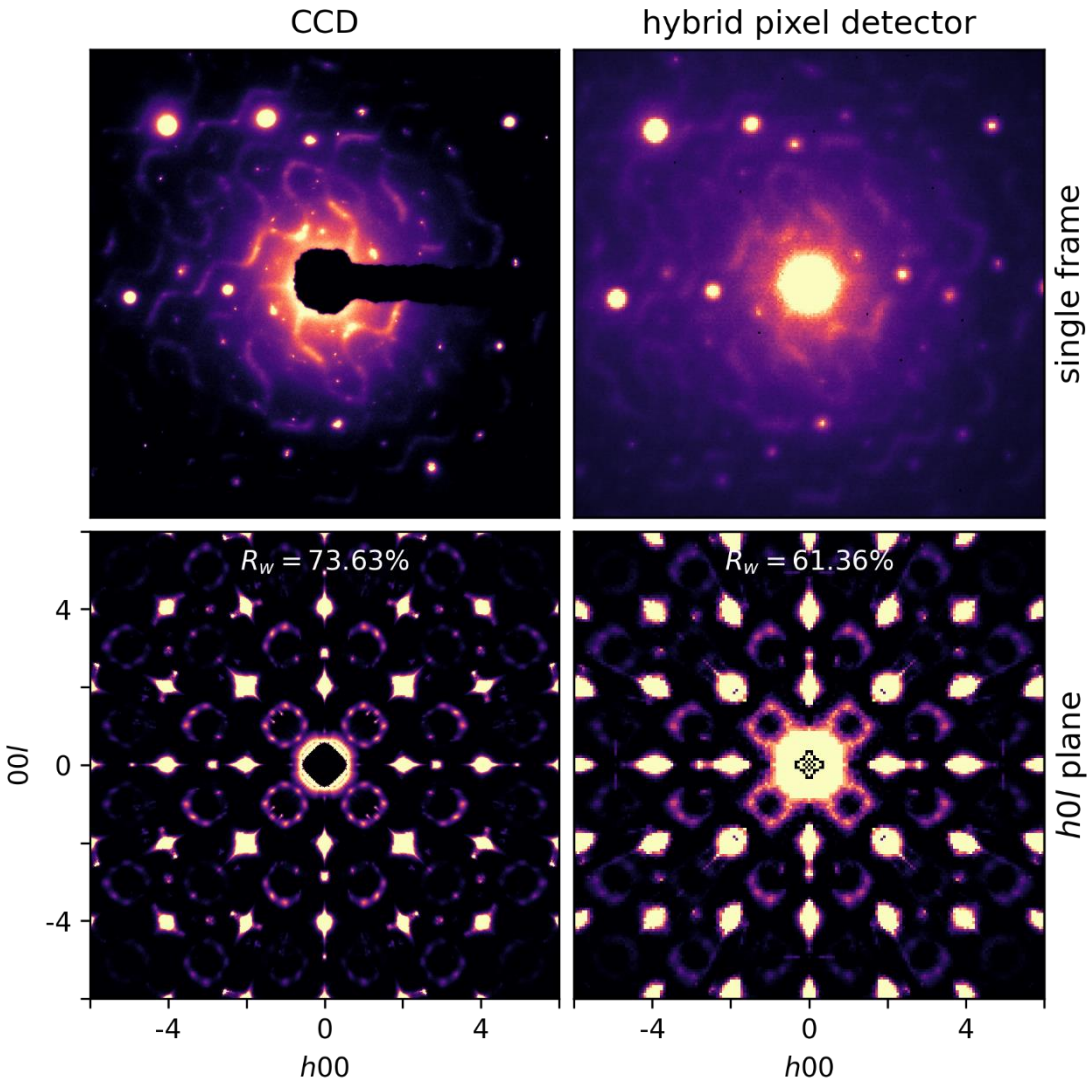

Figure 6 Comparison of the *h0l* plane reconstructed from three-dimensional electron diffraction (3D ED) data acquired with a GATAN US1000XP CCD camera and a Quantum Detectors MerlinEM hybrid pixel detector on the same crystal. Data acquired on the thermally quenched sample (Q-0.84 #2). The black spots on the (202) Bragg reflection in the *h0l* plane reconstructed from 3D ED data acquired with the hybrid pixel detector are due to black pixels on the detector.

The disadvantage of using a CCD is that the dynamic range is lower than for hybrid pixel detectors. Besides, diffuse scattering data collected with a CCD contain sensor intrinsic background noise (Welberry & Weber, 2016). Hybrid pixel detectors optimized for electron diffraction might improve the quality of the observed diffuse scattering in 3D ED data. Unfortunately, within the current study, no such detector was available.

The R value in Equation 1 was calculated for the *h0l* plane reconstructed from 3D ED data acquired with a GATAN US1000XP CCD camera and a Quantum Detectors MerlinEM hybrid pixel detector. Although the resolution of the diffuse scattering acquired with the CCD detector is better, the R value

obtained for the *h0l* plane reconstructed from 3D ED data acquired with the CCD ($R_w = 73.63\%$) is higher than the R value obtained for the *h0l* plane reconstructed from 3D ED data acquired with the hybrid pixel detector ($R_w = 61.36\%$). The higher R value for the *h0l* plane reconstructed from 3D ED data acquired with the CCD can be explained by the presence of sharp satellite reflections on top of the diffuse scattering. The satellite reflections are sharper in the *h0l* plane reconstructed from 3D ED data acquired with the CCD than in the *h0l* plane reconstructed from 3D ED data acquired with the hybrid pixel detector. The satellite reflections are almost absent in the calculated *h0l* plane in Fig. S2, which explains the higher R value for the *h0l* plane reconstructed from 3D ED data acquired with the CCD. The absence of sharp satellite reflections in the calculated *h0l* plane is due to the absence of long-range Nb-vacancy order in the model crystal used for the calculation of the diffuse scattering.

Diffraction patterns acquired with a CMOS detector do not suffer from blooming artefacts and might thus be more ideal for acquiring high-quality diffuse scattering data. Because we have no CMOS detector available in our lab, a comparison between CCD and CMOS detectors is not included in the current study.

3.6. Electron vs. X-ray diffraction

3D ED allows to determine the crystal structure of materials for which no crystals large enough for single-crystal X-ray diffraction are available. The 3D ED data of the slowly cooled sample in Fig. 1, for example, were acquired on a 150 nm sized crystal. Fig. 7 shows the *hhl* plane and the planes 1, 2, 3 and 4 voxels above the *hhl* plane, reconstructed from single-crystal X-ray and 3D ED data acquired on the slowly cooled sample (SC-0.81). Each plane in Fig. 7 has a thickness of one voxel. The *hhl* plane reconstructed from 3D ED data shows additional satellite reflections compared with the *hhl* plane reconstructed from single-crystal X-ray diffraction data (satellite reflections indicated by the white circles). These additional satellite reflections have their maximum intensity in the plane four voxels above the *hhl* plane. The Bragg reflections are broader in the 3D ED data than in the single-crystal X-ray diffraction data, which was also observed in (Schmidt et al., 2023). The resolution of the observed diffuse scattering is thus lower for 3D ED data acquired with a CCD than for single-crystal X-ray diffraction data acquired with a hybrid pixel detector. Consequently, the reflections indicated by the white circles in the *hhl* plane reconstructed from 3D ED are from slightly above and below the *hhl* plane.

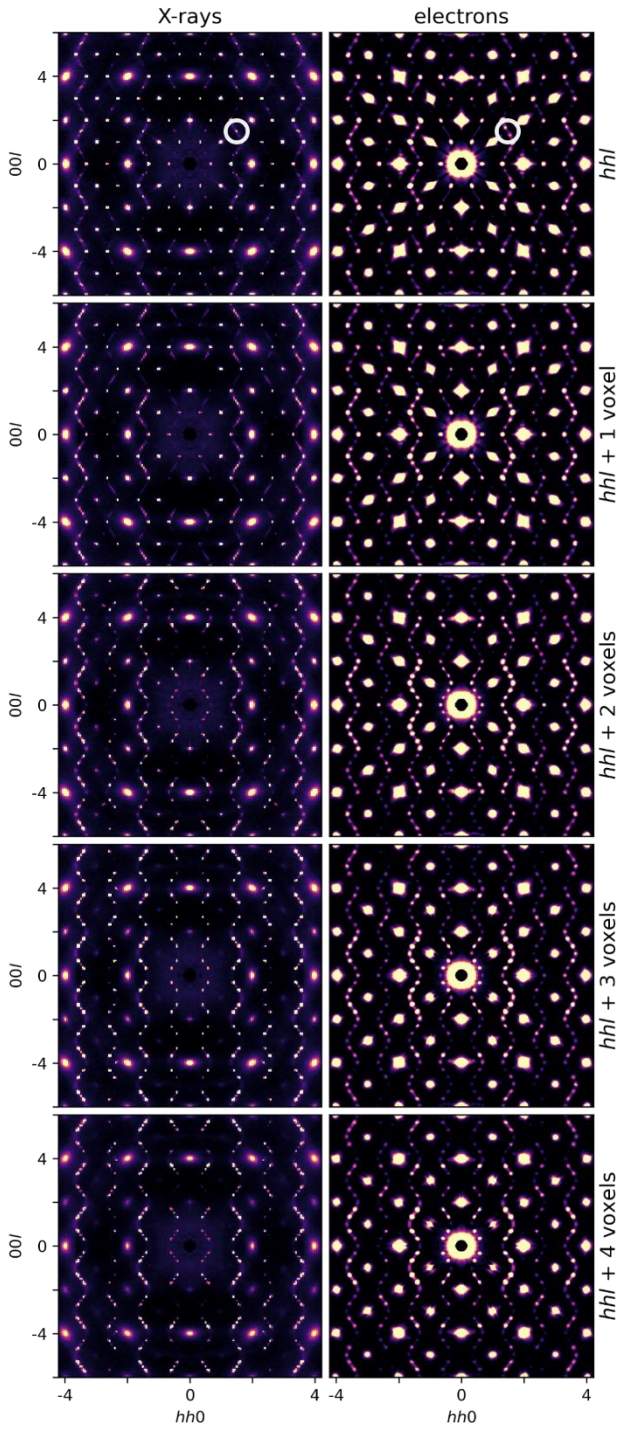

Figure 7 Comparison of the *hhl* plane and the planes 1, 2, 3 and 4 voxels above the *hhl* plane, reconstructed from single-crystal X-ray diffraction and three-dimensional electron diffraction (3D ED) data. The *hhl* plane reconstructed from 3D ED data shows additional satellite reflections compared with the *hhl* plane reconstructed from single-crystal X-ray diffraction data (reflections indicated by the white circles). These additional satellite reflections have their maximum intensity four voxels above the *hhl* plane. Data acquired on the slowly cooled sample (SC-0.81).

The resolution of the diffuse scattering is determined by various effects, including the convergence of the beam, the point spread function of the detector and the crystal mosaicity. Other parameters that may influence the resolution of the observed diffuse scattering are the monochromaticity of the beam, vibrations of the crystal or the instrument, the detector distance and the data collection step width (Boysen & Adlhart, 1987). For high-resolution experiments, 3D ED data should be collected with a step size of 0.1° or smaller, similar as for single-crystal X-ray diffraction (Welberry & Weber, 2016).

To a first approximation, most of these effects broaden Bragg reflections isotropically and uniformly and the resolution function can be approximated by a Gaussian function (Weber & Simonov, 2012). To account for resolution effects during the refinement of local order parameters in *DISCUS* and *Yell*, the intensity of each voxel in the calculated diffuse scattering data should be convoluted with a Gaussian function. The standard deviation of the Gaussian function can be estimated from the intensity profile of unsaturated Bragg reflections. However, angular broadenings caused by e.g., crystal mosaicity and radial broadenings caused by e.g., the spectral width of the beam cannot easily be corrected (Weber & Simonov, 2012).

4. Conclusion

In this article, we showed that the three-dimensional diffuse scattering in three-dimensional electron diffraction (3D ED) data can be obtained with a quality comparable to that from single-crystal X-ray diffraction. The agreement between the observed and calculated diffuse scattering depends on the data acquisition mode, the detector type and the use of an energy filter. We found that diffuse scattering data used for quantitative analysis are preferably acquired in selected area electron diffraction (SAED) mode using a CCD and an energy filter. In contrast to single-crystal X-ray diffraction, the resolution of the observed diffuse scattering is worse for 3D ED data acquired with the Quantum Detectors MerlinEM hybrid pixel detector than for 3D ED data acquired with the GATAN US1000XP CCD, which is caused by a difference in the number of pixels between both detectors and a difference in the detector point spread function. As electron diffraction requires much smaller crystal sizes than X-ray diffraction, this opens up the possibility to investigate the local structure of many technologically relevant materials for which no crystals large enough for single-crystal X-ray diffraction are available.

Acknowledgements: The authors would like to thank Dr. Nikolaj Roth for fruitful discussions and Dr. Lukas Palatinus for providing an option to apply symmetry averaging in the three-dimensional reciprocal lattice in *PETS2*. The authors also acknowledge the Hercules fund 'Direct electron detector for soft matter TEM' from Flemish Government for the purchase of the Merlin detector.

Author contributions: Romy Poppe: Data collection; data processing; visualisation; writing – original draft; writing – review and editing. Joke Hadermann: conceptualization; writing – review and editing; resources; funding acquisition.

References:

Boysen, H. & Adlhart, W. (1987). *J Appl Crystallogr* **20**, 200–209.

Brázda, P., Palatinus, L., Drahokoupil, J., Knížek, K. & Buršík, J. (2016). *Journal of Physics and Chemistry of Solids* **96**, 10–16.

Fujii, Y., Miura, H., Suzuki, N., Shoji, T. & Nakayama, N. (2007). *Solid State Ion* **178**, 849–857.

Gemmi, M., Mugnaioli, E., Gorelik, T. E., Kolb, U., Palatinus, L., Boullay, P., Hovmöller, S. & Abrahams, J. P. (2019). *ACS Cent Sci* **5**, 1315–1329.

Gimenez, E. N., Ballabriga, R., Campbell, M., Horswell, I., Llopart, X., Marchal, J., Sawhney, K. J. S., Tartoni, N. & Turecek, D. (2011). *IEEE Trans Nucl Sci* **58**, 323–332.

Goodwin, A. L., Withers, R. L. & Nguyen, H. B. (2007). *Journal of Physics Condensed Matter* **19**, 335216.

Gorelik, T. E., Bekő, S. L., Teteruk, J., Heyse, W. & Schmidt, M. U. (2023). *Acta Crystallogr B Struct Sci Cryst Eng Mater* **79**, 122–137.

Jakůbek, J. (2009). *Journal of Instrumentation* **4**, https://doi.org/10.1088/1748-0221/4/03/P03013.

Kolb, U., Gorelik, T., Kübel, C., Otten, M. T. & Hubert, D. (2007). *Ultramicroscopy* **107**, 507–513.

Kolb, U., Gorelik, T. & Otten, M. T. (2008). *Ultramicroscopy* **108**, 763–772.

Kraft, P., Bergamaschi, A., Broennimann, C., Dinapoli, R., Eikenberry, E. F., Henrich, B., Johnson, I., Mozzanica, A., Schlepütz, C. M., Willmott, P. R. & Schmitt, B. (2009). *J Synchrotron Radiat* **16**, 368–375.

Krysiak, Y., Barton, B., Marler, B., Neder, R. B. & Kolb, U. (2018). *Acta Crystallogr A Found Adv* **74**, 93–101.

Krysiak, Y., Marler, B., Barton, B., Plana-Ruiz, S., Gies, H., Neder, R. B. & Kolba, U. (2020). *IUCrJ* **7**, 522–534.

Neagu, A. & Tai, C. W. (2017). *Sci Rep* **7**, 1–12.

Palatinus, L., Brázda, P., Jelínek, M., Hrdá, J., Steciuk, G. & Klementová, M. (2019). *Acta Crystallogr B Struct Sci Cryst Eng Mater* **75**, 512–522.

Pangaud, P., Basolo, S., Boudet, N., Berar, J. F., Chantepie, B., Clemens, J. C., Delpierre, P., Dinkespiler, B., Medjoubi, K., Hustache, S., Menouni, M. & Morel, C. (2008). *Nucl Instrum Methods Phys Res A* **591**, 159–162.

Poppe, R., Roth, N., Neder, R. B., Palatinus, L., Iversen, B. B. & Hadermann, J. (2024). *IUCrJ* **11**, 82–91.

Poppe, R., Vandemeulebroucke, D., Neder, R. B. & Hadermann, J. (2022*a*). *IUCrJ* **9**, 695–704.

Poppe, R., Vandemeulebroucke, D., Neder, R. B. & Hadermann, J. (2022*b*). *IUCrJ* **9**, 695–704.

Proffen, T. & Neder, R. B. (1997). *J Appl Crystallogr* **30**, 171–175.

Roth, N., Beyer, J., Fischer, K. F. F., Xia, K., Zhu, T. & Iversen, B. B. (2021). *IUCrJ* **8**, 695–702.

Schaub, P., Weber, T. & Steurer, W. (2007). *Philosophical Magazine* **87**, 2781–2787.

Schmidt, E. M., Klar, P. B., Krysiak, Y., Svora, P., Goodwin, A. L. & Palatinus, L. (2023*a*). *Nat Commun* **14**, 6512.

Schmidt, E. M., Klar, P. B., Krysiak, Y., Svora, P., Goodwin, A. L. & Palatinus, L. (2023*b*). *Nat Commun* **14**, 6512.

Vincent, R. & Midgley, P. a. (1994). *Ultramicroscopy* **53**, 271–282.

Wang, B. (2019). Development of rotation electron diffraction as a fully automated and accurate method for structure determination. Stockholm University.

Weber, T. & Simonov, A. (2012). *Zeitschrift Fur Kristallographie* **227**, 238–247.

Welberry, T. R. & Goossens, D. J. (2016). *IUCrJ* **3**, 309–318.

Welberry, T. R. & Weber, T. (2016). *Crystallogr Rev* **22**, 2–78.

Withers, R. L., Welberry, T. R., Brink, F. J. & Norén, L. (2003). *J Solid State Chem* **170**, 211–220.

Withers, R. L., Welberry, T. R., Larsson, A. K., Liu, Y., Norén, L., Rundlöf, H. & Brink, F. J. (2004). *J Solid State Chem* **177**, 231–244.

Xia, K., Nan, P., Tan, S., Wang, Y., Ge, B., Zhang, W., Anand, S., Zhao, X., Snyder, G. J. & Zhu, T. (2019). *Energy Environ Sci* **12**, 1568–1574.

Yang, T., Xu, H., Zou, X. & Borbély, A. (2022). *J Appl Crystallogr* **55**, 1583–1591.

Zeier, W. G., Anand, S., Huang, L., He, R., Zhang, H., Ren, Z., Wolverton, C. & Snyder, G. J. (2017). *Chemistry of Materials* **29**, 1210–1217.

Zhao, H., Krysiak, Y., Hoffmann, K., Barton, B., Molina-Luna, L., Neder, R. B., Kleebe, H. J., Gesing, T. M., Schneider, H., Fischer, R. X. & Kolb, U. (2017). *J Solid State Chem* **249**, 114–123.

Zuo, J. M., Gao, M., Tao, J., Li, B. Q., Twesten, R. & Petrov, I. (2004). *Microsc Res Tech* **64**, 347–355.

Supporting Information:

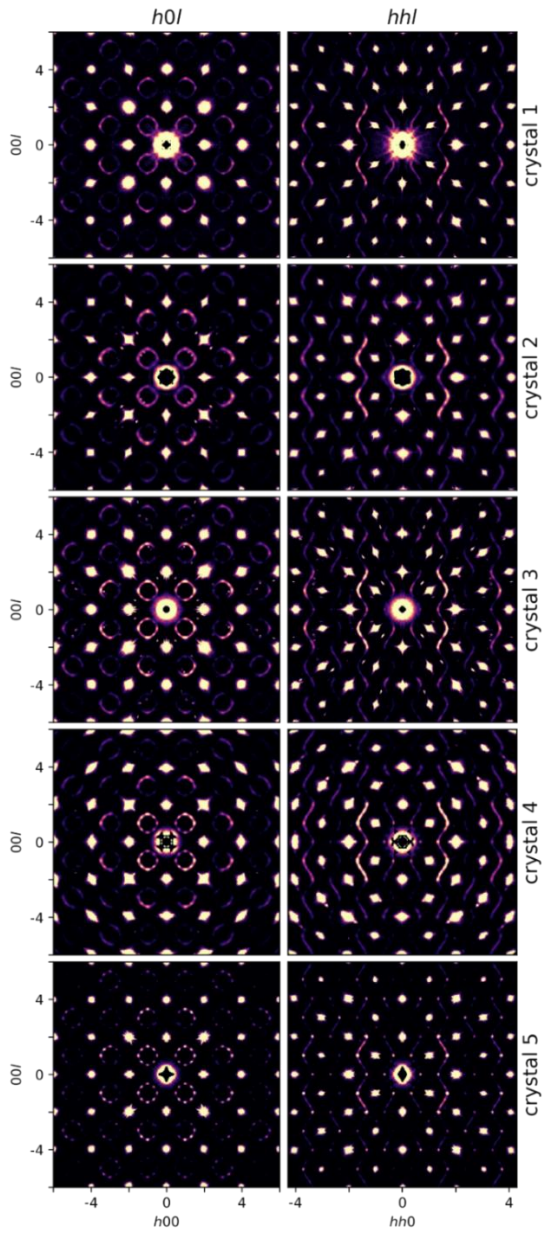

Figure S1 Comparison of the *h0l* and *hhl* planes reconstructed from three-dimensional electron diffraction (3D ED) data acquired on five different crystals of the thermally quenched sample (Q-0.84 #2). The angular broadening of the Bragg reflections is different for each crystal, which is due to differences in the crystal mosaicity. The crystals consist of domains in which the lattice planes are slightly misaligned. The larger the spread of lattice plane orientations, the larger the mosaicity. The additional reflections between the Bragg reflections for crystals 2 and 3 are due to neighbouring crystals. Due to symmetry averaging with Laue class $m\bar{3}m$, each additional reflection in the *h0l* plane will appear eight times, while each additional reflection in the *hhl* plane will appear four times.

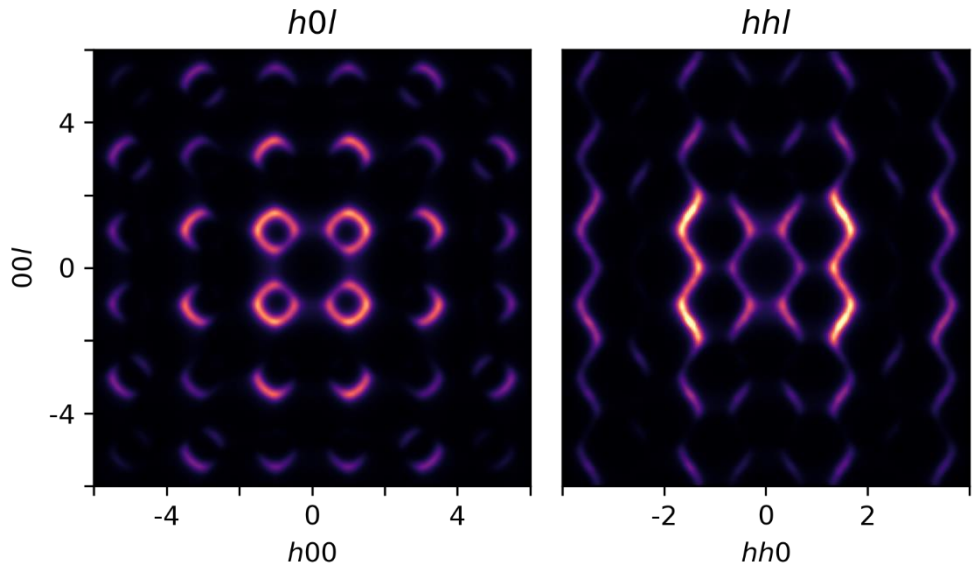

Figure S2 Diffuse scattering in the *h0l* and *hhl* planes calculated for the short-range order parameters previously refined using a Monte Carlo refinement in *DISCUS*. The calculated *h0l* plane was published in (Poppe *et al.*, 2024).

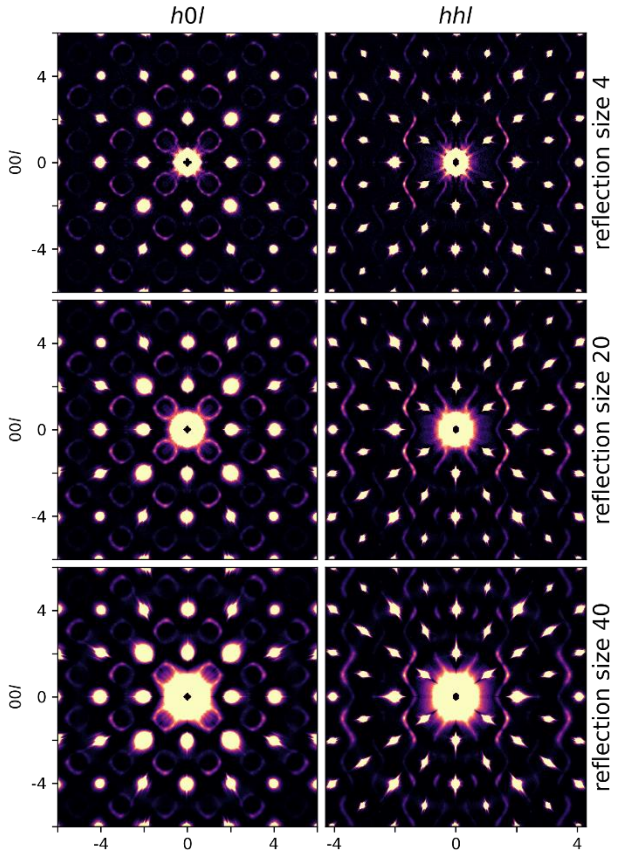

Figure S3 Comparison of the *h0l* and *hhl* planes reconstructed for a reflection size of respectively 4, 20 and 40 pixels. When the reflection size is much lower (e.g. 4 pixels) than the width of the diffuse scattering contours (20 pixels), part of the elastic diffuse scattering will be subtracted. Data acquired on the thermally quenched sample (Q-0.84 #2).

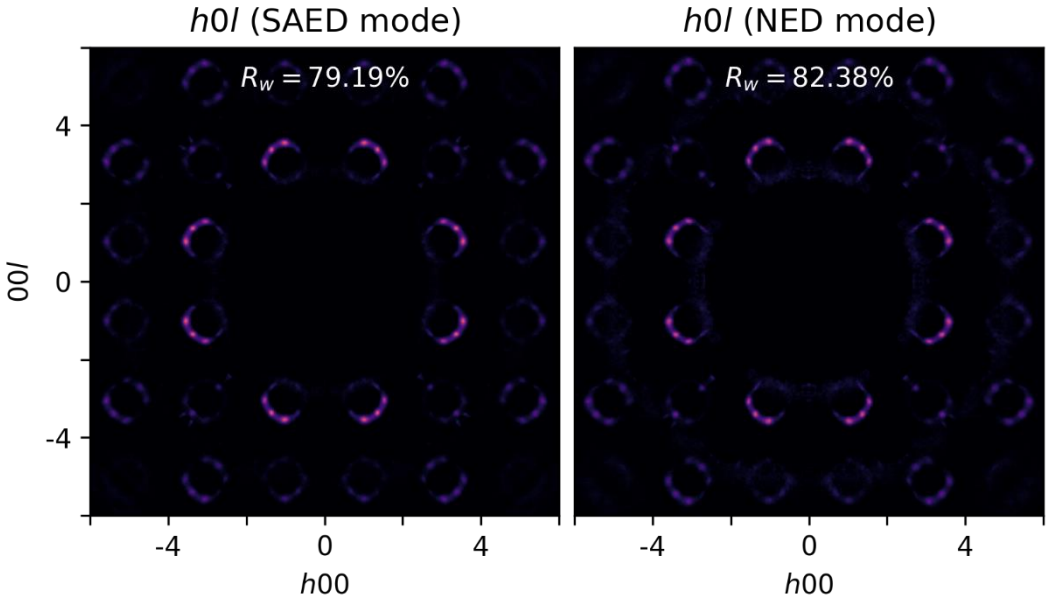

Figure S4 Comparison of the *h0l* planes reconstructed from three-dimensional electron diffraction (3D ED) data acquired in selected area electron diffraction (SAED) and nano electron diffraction (NED) mode. The Bragg reflections and the diffuse scattering close to the central beam have been subtracted to calculate the R value. Data acquired on the thermally quenched sample (Q-0.84 #2).

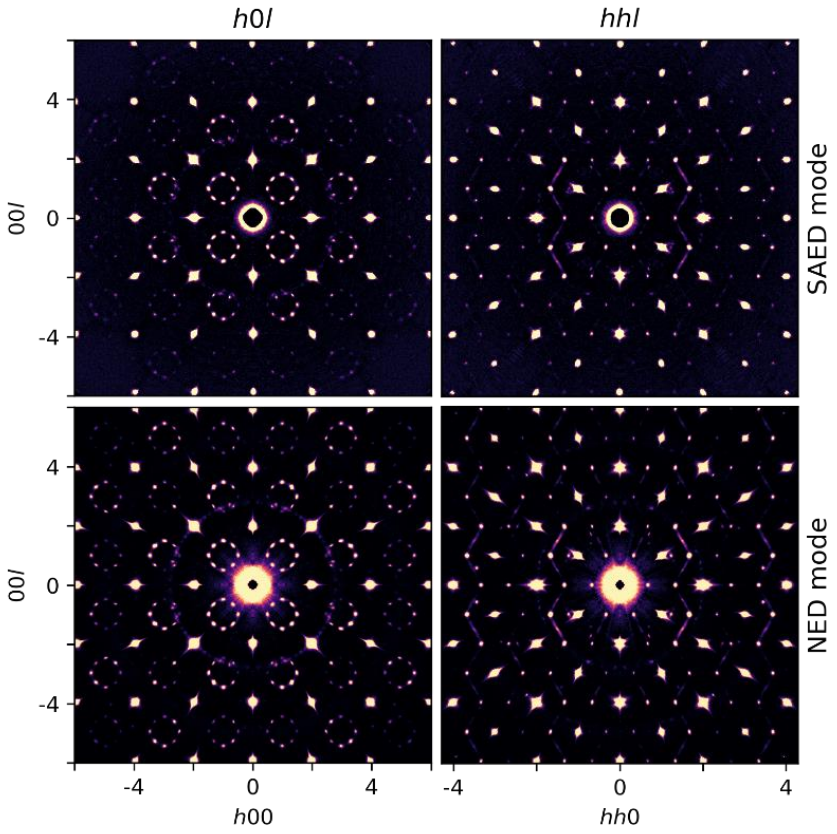

Figure S5 Comparison of the *h0l* and *hhl* planes reconstructed from three-dimensional electron diffraction (3D ED) data acquired in selected area electron diffraction (SAED) and nano electron diffraction (NED) mode. Data acquired on the slowly cooled sample (SC-0.81).